

Learning to Predict the Cosmological Structure Formation

Siyu He^{a,b,c}, Yin Li^{d,e,f}, Yu Feng^{d,e}, Shirley Ho^{c,e,d,a,b}, Siamak Ravanbakhsh^g, Wei Chen^c, and Barnabás Póczos^h

^aCarnegie Mellon University, 5000 Forbes Avenue, Pittsburgh PA 15213, USA; ^bMcWilliams Center for Cosmology, Carnegie Mellon University, Pittsburgh, PA 15213, USA; ^cCenter for Computational Astrophysics, Flatiron Institute, 162 5th Ave, New York, NY 10010, USA; ^dBerkeley Center for Cosmological Physics, University of California, Berkeley, CA 94720, USA; ^eLawrence Berkeley National Laboratory, Berkeley, CA 94720, USA; ^fKavli Institute for the Physics and Mathematics of the Universe (WPI), UTIAS, The University of Tokyo, Chiba 277-8583, Japan; ^gComputer Science Department, University of British Columbia, Vancouver, BC V6T1Z4, Canada; ^hMachine Learning Department, Carnegie Mellon University, 5000 Forbes Ave., Pittsburgh, PA 15213, USA

Matter evolved under influence of gravity from minuscule density fluctuations. Non-perturbative structure formed hierarchically over all scales, and developed non-Gaussian features in the Universe, known as the Cosmic Web (1). To fully understand the structure formation of the Universe is one of the holy grails of modern astrophysics. Astrophysicists survey large volumes of the Universe (2–9) and employ a large ensemble of computer simulations to compare with the observed data in order to extract the full information of our own Universe. However, to evolve trillions of galaxies over billions of years even with the simplest physics is a daunting task. We build a deep neural network, the Deep Density Displacement Model (hereafter D^3M), to predict the non-linear structure formation of the Universe from simple linear perturbation theory. Our extensive analysis, demonstrates that D^3M outperforms the second order perturbation theory (hereafter 2LPT), the commonly used fast approximate simulation method, in point-wise comparison, 2-point correlation, and 3-point correlation. We also show that D^3M is able to accurately extrapolate far beyond its training data, and predict structure formation for significantly different cosmological parameters. Our study proves, for the first time, that deep learning is a practical and accurate alternative to approximate simulations of the gravitational structure formation of the Universe.

cosmology | deep learning | simulation |

At its core, modeling structure formation of the Universe is a computationally challenging task; it involves evolving trillions of particles with the correct physical model over a large volume over billions of years. To simplify this task, we either simulate a large volume with simpler physics or a smaller volume with more complex physics. In order to produce the cosmic web in large volume, we select gravity, the most important component of the theory, to simulate at large scales. A gravity-only N -body simulation is the most popular; and effective numerical method to predict the full 6D phase space distribution of a large number of massive particles whose positions and velocities evolve over time in the Universe (10). Nonetheless, N -body simulations are relatively computationally expensive, thus making the comparison of the N -body simulated large-scale structure (of different underlying cosmological parameters) with the observed Universe a challenging task. Here, we propose to learn a deep model that predicts the structure formation as an alternative to expensive N -body simulations.

Deep learning (11) is a fast growing branch of machine learning where recent advances have lead to models that reach and sometimes exceed human performance across diverse areas, from analysis and synthesis of images (12–14), sound (15, 16), text (17, 18) and videos (19, 20) to complex control and

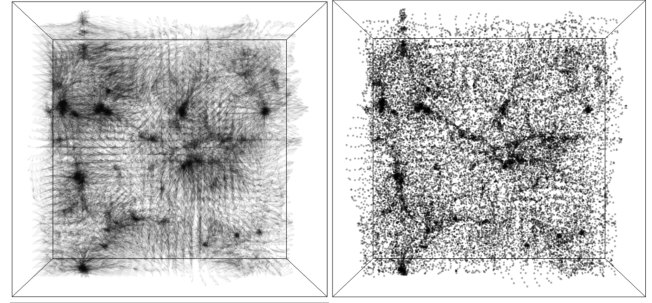


Fig. 1. (left) the displacement vector-field produced by D^3M and; (right) the resulting density field. The vectors in the left figure are uniformly scaled down for better visualization.

planning tasks as they appear in robotics and game-play (21–23). This new paradigm is also significantly impacting a variety of domains in the sciences, from biology (24, 25) to chemistry (26, 27) and physics (28, 29). In particular, in astronomy and cosmology, a growing number of recent studies are using deep learning for a variety of tasks, ranging from analysis of cosmic microwave background (30–32), large-scale structure (33, 34), and gravitational lensing effects (35, 36) to classification of different light sources (37–39).

The ability of these models to learn complex functions has motivated many to use them to understand the physics of interacting objects leveraging image, video and relational data (40–50). However, modeling the dynamics of billions of particles in N -body simulations poses a distinct challenge.

In this paper we show that a variation on the architecture of a well-known deep learning model (51), can efficiently transform the first order approximations to the displacement field and approximate the exact solution, thereby producing accurate estimates of the large-scale structure. Our objective is to show that this approach is a serious contender in replacing expensive cosmological simulations, and to this end we provide an extensive analysis of the results in the following section.

The outcome of a typical N -body simulation depends on both the initial conditions and cosmological parameters. We report a rather surprising observation that our Deep Density Displacement Model (D^3M), trained using a “single” set of

S.He has led the project. S.He, Y.Li, Y.Feng and S.Ho performed the data analysis. Y.Feng provided all the simulations. W.Chen helped build the deep learning model. S.Ravanbakhsh, B.Póczos and W.Chen provided many deep learning suggestions. Y.Feng and S.Ho conceived the idea of using deep learning model to learn the structure formation of the universe. S.Ravanbakhsh, Y.Li, S.Ho and S.He contributed most to the manuscript writing. All authors commented on the manuscript.

Authors declare no competing financial interests.

²To Siyu He correspondence should be addressed. E-mail: siyuh@andrew.cmu.edu

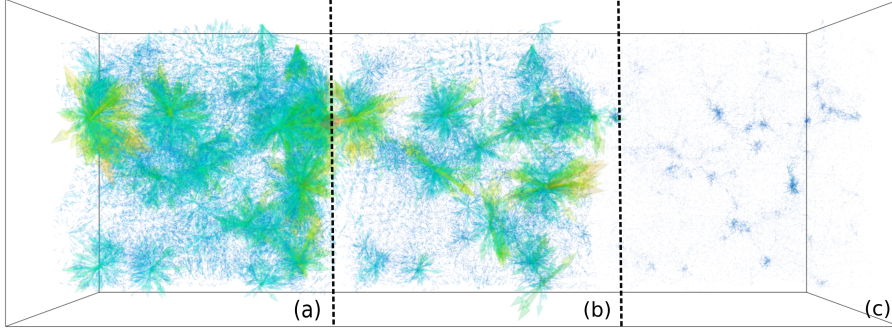


Fig. 2. Error vector for:
 (a) Zel'dovich approximation (ZA): a simple linear model that evolves particle along the initial velocity vector;
 (b) second order Lagrangian perturbation theory (2LPT): a commonly used approximate N-body simulation method;
 (c) deep learning (D³M).
 Each vectors indicates the difference between the target location and produced approximation, scaled up (by a factor of 5) for better visualization. Predictions of FastPM serves as the ground truth.

cosmological parameters can generalize to new set of significantly different parameters, minimizing the need for training data on diverse range of parameters in practical settings.

Setup

We build a deep neural network, Deep Density Displacement Model (D³M) with similar input and output variables of an N -body simulation. The input to our D³M is the displacement field from the so called Zel'dovich Approximation(52) (hereafter ZA). A displacement vector is the difference in particle position between target redshift $z = 0$, i.e., the present time, and it's Lagrangian position on a uniform grid. ZA evolves the particles on linear trajectories along their initial displacements. It is accurate when the displacement is small, therefore is frequently used to construct the initial conditions of N -body simulations (53).

As the ground truth, the target displacement field is produced using FastPM (54), a recent approximate N-body simulation scheme that is based on a particle-mesh (PM) solver. FastPM quickly approaches a full N-body simulation with high accuracy and provides a viable alternative for exact N-body simulations for the purpose of our study.

A significantly faster approximation to N-body simulations, is produced by second-order Lagrangian perturbation theory (hereafter 2LPT), which bends each particle's trajectory with a quadratic correction (55). Many cosmological analyses use 2LPT to generate a large number of cosmological simulations for comparison of astronomical dataset against the physical model (56, 57) or to compute the covariance of the dataset (58–60). We regard 2LPT as an effective way to generate a relatively correct description of the large-scale structure and therefore, this method serves as a natural competitor to D³M.

We generate 10,000 pairs of ZA approximations as input and accurate FastPM approximations as target. We use simulations of 32^3 N -body particles in a volume of 128 Mpc/h (600 million light years) on each side. The particles have a mean separation of 4 Mpc/h per dimension.

Displacement versus Density Field. An important choice in our approach is training with displacement field rather than density field. Displacement field Ψ and density field ρ are two ways of describing the same distribution of particles, and they are related by the law of mass conservation. The mean value of the density field is $\bar{\rho}$, relative to which the density fluctuation can be described by the over-density field, $\delta = \rho/\bar{\rho} - 1$.

When the displacement field is small and curl-less, the

choice of density vs displacement field for the output of the model is irrelevant, as there is a bijective mapping between these two representations. However as the displacement grow into the non-linear regime of structure formation, different displacement fields can produce identical density fields. (e.g. 61) Therefore, providing the model with the target displacement field during the training is significantly more informative as it does not have the ambiguity associated with the density field. Indeed we could not produce comparable results when using the density field as our input and target.

Results and Analysis

Figure 1 shows the displacement vector field as predicted by D³M (left) and the point-cloud representation of the predicted structure formation (right). It is possible to identify structures such as clusters, filaments and voids in this point-cloud representation. In the following we quantify the accuracy of D³M and compare its performance to 2LPT.

Point-Wise Comparison. Let the rank four tensors $\Psi \in \mathbb{R}^{d \times d \times d \times 3}$ denote the displacement field, where d is the number of spatial resolution elements per side ($d = 32$). A natural error measure is the norm of the error $e = \hat{\Psi} - \Psi_t$, where Ψ_t is the true displacement field (FastPM) and $\hat{\Psi}$ is the prediction (ZA, 2LPT or D³M). Figure 2 compares this error for different approximations in a single simulation. We observe that D³M predictions are very close to the ground truth, with a maximum error of 4.46 Mpc/h over all 1000 simulations. For 2LPT this number is significantly higher at 15.20 Mpc/h.

Since a few large error vectors can dominate the L2 norm, we also measure the relative displacement error $|\hat{\Psi} - \Psi_t|/|\Psi_t|$. Using this measure we observe the same pattern: D³M is almost 3 times more accurate than 2LPT. In particular, D³M is able to achieve an average of 2.8% in relative displacement error per voxel on test data, while 2LPT can only achieve 9.3%.

2-Point Correlation Comparison. As suggested by Figure 2 the more dense regions seem to have a higher error for all methods – that is the error is larger when the structure formation is more non-linear for both D³M and 2LPT. This correlation of error with scale is captured in 2-point and 3-point correlation analysis.

Cosmologists often employ compressed summary statistics of the density field in their studies. The most widely used of these statistics is 2-point correlation function (2PCF) $\xi(r)$

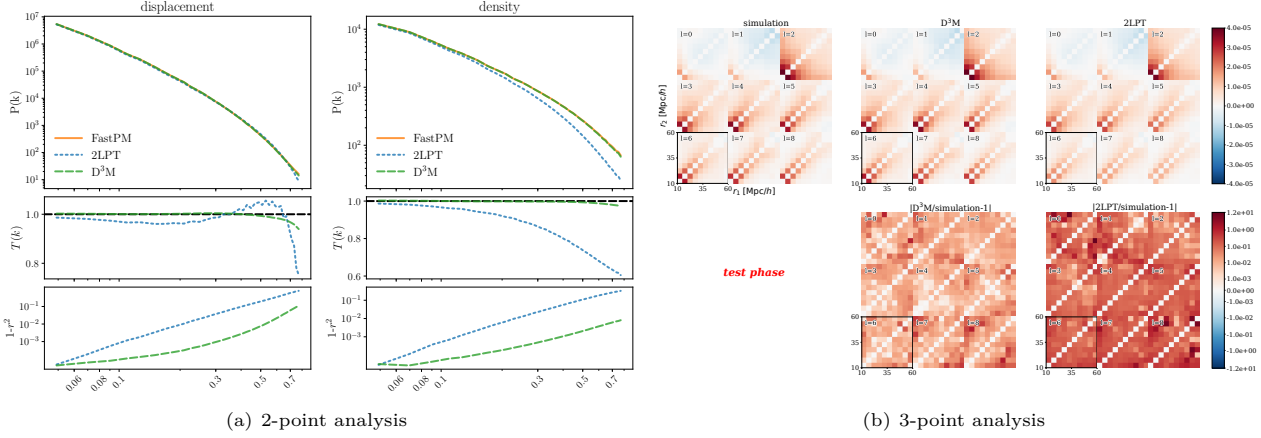


Fig. 3. (a) From top to bottom: (top) density and displacement power-spectrum of D³M, 2LPT, and FastPM; (middle) transfer function – i.e., the square root of the ratio of the predicted power-spectrum and the ground truth, and; (bottom) $1-r^2$ where r is the correlation coefficient between the predicted fields and the true fields. Results are the averaged values from 1000 test simulations.

(b) 3-point correlation function measured as binned multipole coefficients $\zeta_l(r_1, r_2)$. Results are averaged values from 10 test simulations. The top panel shows $\zeta_l(r_1, r_2)$ for D³M, FastPM, and 2LPT. In order to amplify the finer features, we have weighted $\zeta_l(r_1, r_2)$ by $r_1^2 r_2^2 / (100 \text{ Mpc/h})^4$ in each spherical shell. On the diagonal elements, the 3PCF is expected to be dominated by squeezed triangles for which perturbation theory is not valid, so we have not computed the diagonal elements (thus blank in the plots here). The bottom panel shows the relative residual of D³M and 2LPT models compared to FastPM.

and its Fourier transform, the power spectrum $P(k)$:

$$\begin{aligned} \xi(|\mathbf{r}|) &= \langle \delta_A(\mathbf{r}') \delta_B(\mathbf{r}' + \mathbf{r}) \rangle, \\ P(|\mathbf{k}|) &= \int d^3\mathbf{r} \, \xi(r) e^{i\mathbf{k} \cdot \mathbf{r}}, \end{aligned} \quad [1]$$

where the ensemble average $\langle \rangle$ is taken over all possible realizations of the Universe. Our Universe is observed to be homogeneous and isotropic on large scales, i.e. without any special location or direction. This allows one to drop the dependences on \mathbf{r}' and on the direction of \mathbf{r} , leaving only the amplitude $|\mathbf{r}|$ in the final definition of $\xi(r)$. In the second equation, $P(k)$ is simply the Fourier transform of $\xi(r)$, and captures the dispersion of the plane wave amplitudes at different scales in the Fourier space. \mathbf{k} is the 3D wavevector of the plane wave, and its amplitude k (the wavenumber) is related to the wavelength λ by $k = 2\pi/\lambda$. Due to isotropy of the Universe, we drop the vector form of \mathbf{r} and \mathbf{k} when we discuss $\xi(r)$ and $P(k)$ from here onwards.

We focus on the Fourier-space representation of the 2-point correlation. We employ the transfer function $T(k)$ and the correlation coefficient $r(k)$ as metrics to quantify the model performance against the ground truth (FastPM) on the 2-point correlation. We define the transfer function $T(k)$ as the square root of the ratio of two power spectra,

$$T(k) = \sqrt{\frac{P_{\text{pred}}(k)}{P_{\text{true}}(k)}}, \quad [2]$$

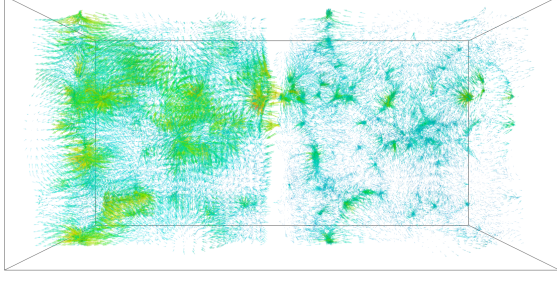
where $P_{\text{pred}}(k)$ is the density or displacement power spectrum from 2LPT or D³M predictions, and $P_{\text{true}}(k)$ is the equivalent from the ground truth (FastPM). The correlation coefficient $r(k)$ is a form of normalized cross power spectrum,

$$r(k) = \frac{P_{\text{pred} \times \text{true}}(k)}{\sqrt{P_{\text{pred}}(k) P_{\text{true}}(k)}}, \quad [3]$$

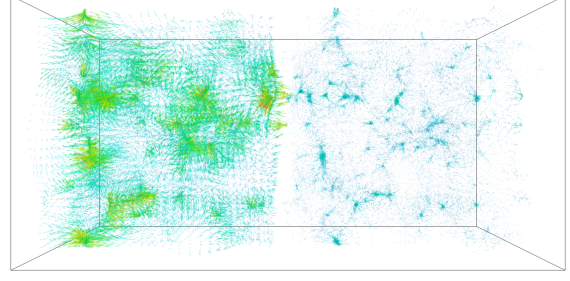
where $P_{\text{pred} \times \text{true}}(k)$ is the cross power spectrum between 2LPT or D³M predictions and the ground truth (FastPM) simulation. Transfer function captures the discrepancy in amplitudes,

while the correlation coefficient can indicate the discrepancy in phases as functions of scales. For a perfectly accurate prediction, $T(k)$ and $r(k)$ are both 1. In particular, $1-r^2$ describes stochasticity, the fraction of the variance in the prediction that cannot be explained by the true model.

Figures 3(a) shows the average power spectrum, transfer function $T(k)$ and stochasticity $1-r^2(k)$ of the displacement field and the density field over 1000 simulations. The power spectrum of density from 2LPT prediction is 3% smaller than that of FastPM on large scales ($k \approx 0.05 \text{ h/Mpc}$). This is expected since 2LPT performs accurately only on very large scales ($k < 0.01 \text{ h/Mpc}$). The displacement transfer function of 2LPT increases above 1 at $k \approx 0.35 \text{ h/Mpc}$ and then drops sharply. The increase of 2LPT displacement transfer function is because 2LPT over-estimates the displacement power at small scales (see, e.g. 62). There is a sharp drop of power near the voxel scale, as we smooth over voxel scales in our predictions, which automatically erases power at scales smaller than the voxel size. Now we turn to D³M predictions: both the density and displacement transfer functions of the D³M differ from 1 by a mere 0.4% at scale $k \lesssim 0.4 \text{ h/Mpc}$, and this discrepancy only increases to 3% and 6% for density field and displacement field respectively, as k increases to the Nyquist frequency around 0.7 h/Mpc . The stochasticity hovers at approximately 10^{-3} and 10^{-2} for most scales. In other words, the correlation coefficient of either density or displacement field is over 90% between the D³M predictions and FastPM simulations all the way down to small scales of $k = 0.7 \text{ h/Mpc}$. The transfer function and correlation coefficient of the D³M suggest its nearly perfect predicting power from large to intermediate scales — the regimes where traditional perturbation theories like the 2LPT work reasonably well — and even beyond. Only on fairly small scales that the D³M starts to falter, which is not surprising as the deeply nonlinear evolution at these scales is also the most difficult to solve accurately in simulations and even impossible for any analytical theories to model.



(a) Changing primordial amplitude of scalar perturbations



(b) Changing matter density

Fig. 4. (a) the vector fields show the difference between displacement field for A_0 and two extremes of $A_s = .2A_0$ (left) and $A_s = 1.8A_0$ (right). While the difference for smaller value of A_s is larger, the displacement for larger A_s is more non-linear. This nonlinearity due to concentration of mass makes the prediction more difficult. (b) a similar comparison showing the difference between the displacement field for smaller and larger values of $\Omega_m \in \{.1, .5\}$ and $\Omega_m = 0.3089$ that was used for training.

3-Point Correlation Comparison. The 3-point correlation function (3PCF) measures the correlation among the field of interest at 3 locations in the configuration space, which is equivalently defined as bispectrum in Fourier space. Here we concentrate on the 3PCF due to computational convenience:

$$\zeta(r_1, r_2, \theta) = \langle \delta(\mathbf{x})\delta(\mathbf{x} + \mathbf{r}_1)\delta(\mathbf{x} + \mathbf{r}_2) \rangle. \quad [4]$$

where $r_1 = |\mathbf{r}_1|$ and $r_2 = |\mathbf{r}_2|$. Translation invariance guarantees that ζ is independent of \mathbf{x} . Rotational symmetry further eliminates all direction dependence but that on θ , the angle between \mathbf{r}_1 and \mathbf{r}_2 . The multipole moments of $\zeta(r_1, r_2, \theta)$, $\zeta_\ell(r_1, r_2) = (2\ell + 1) \int d\theta P_\ell(\cos \theta) \zeta(r_1, r_2, \theta)$ where $P_\ell(\cos \theta)$ is the Legendre polynomial of degree ℓ , can be efficiently estimated with pair counting (63). While the input variables (ZA) does not contain significant correlations beyond the second order (power spectrum level), we expect our D³M to be capable of generating densities with a 3PCF that mimics that of ground truth.

We compare the 3PCF calculated from FastPM, 2LPT and D³M by analyzing the 3PCF through the multipole moments $\zeta_\ell(r_1, r_2)$. Figure 3(c) shows the binned multipole coefficients $\zeta_\ell(r_1, r_2)$ of the 3PCF. We used 10 radial bins with $\Delta r = 5 \text{ Mpc/h}$. The upper panel in Figure 3(c) shows the average $\zeta_\ell(r_1, r_2)$ over 10 simulations. $\ell = 2$ contributes the largest amplitude contribution to the 3PCF, especially for triangles that are not close to squeezed configuration (two sides of very similar amplitude). For $\ell \geq 3$, the amplitude of 3PCF near the diagonal dominates. For higher multipoles, $\zeta_\ell \sim 1/(r_1^2 r_2^2) + 1/(r_1^2 r_3^2) + 1/(r_2^2 r_3^2)$, thus the amplitude is dominated by a small population of squeezed triangles where two sides are equal and the third side near 0 (63). To compare the performance of D³M and 2LPT predictions, we show the relative residual of D³M prediction and 2LPT with regard to FastPM in the lower panel in Figure. 3(c). The difference between FastPM and D³M is notably smaller than that between FastPM and 2LPT at all angular scales. To quantify our comparison further, we calculate the relative 3PCF residual defined as

$$\begin{aligned} & \text{3PCF relative residual} \\ &= \frac{1}{9 \times N_r} \sum_{\ell=0}^8 \sum_{r_1, r_2} \frac{|\zeta_\ell(r_1, r_2)_{\text{pred}} - \zeta_\ell(r_1, r_2)_{\text{true}}|}{|\zeta_\ell(r_1, r_2)_{\text{true}}|} \quad [5] \end{aligned}$$

where N_r is the number of (r_1, r_2) bins. The mean relative

3PCF residual of D³M prediction and 2LPT compared to FastPM is 0.79% and 7.82% respectively. The D³M performance on 3PCF is also an order of magnitude better than 2LPT, which indicates the D³M is far better at capturing the non-Gaussian structure formation.

Generalizing to New Cosmological Parameters

So far, we trained our model using a “single” choice of cosmological parameters $A_s = 2.142 \times 10^{-9}$ (hereafter $A_0 = 2.142 \times 10^{-9}$) and $\Omega_m = 0.3089$ (64). A_s is the primordial amplitude of the scalar perturbation from cosmic inflation, and Ω_m is the fraction of the total energy density that is matter at the present time, and we will call it matter density parameter for short. The true exact value of these parameters are unknown and different choices of these parameters change the large-scale structure of the Universe; see Figure 4.

Here, we report an interesting observation: D³M trained on a single set of parameters, can predict the structure formation for widely different choices of A_s and Ω_m . These results give important insight about structure formation that we will discuss shortly. From the computational point of view this indicates the possibility of producing simulations for a diverse range of parameters, with minimal training data.

Varying Primordial Amplitude of Scalar Perturbations A_s . After training the D³M using $A_s = A_0$, we change our A_s in the input of our test set by nearly one order of magnitude: $A_s = 1.8A_0$ and $A_s = 0.2A_0$. Again, we use 1000 simulations for analysis of each test case. The average relative displacement error of D³M remains less than 4% per voxel (compared to < 3% when train and test data have the same parameters). This is still well below the error for 2LPT, which is 15.5% and 6.3% for respectively smaller and larger values of A_s .

Figure 5(a) shows the average power spectrum, transfer function and correlation coefficient for both D³M and 2LPT. Overall, D³M performs much better than 2LPT for $A_s = 1.8A_0$. For small $A_s = 0.2A_0$, 2LPT does a better job at predicting the density transfer function and correlation coefficient at the largest scales, otherwise D³M predictions outperforms 2LPT at scales larger than $k = 0.08 \text{ h/Mpc}$. We observe a similar trend with 3PCF analysis: the 3PCF of D³M predictions is notably better than 2LPT ones for larger A_s , compared to smaller A_s where it is only slightly better. These

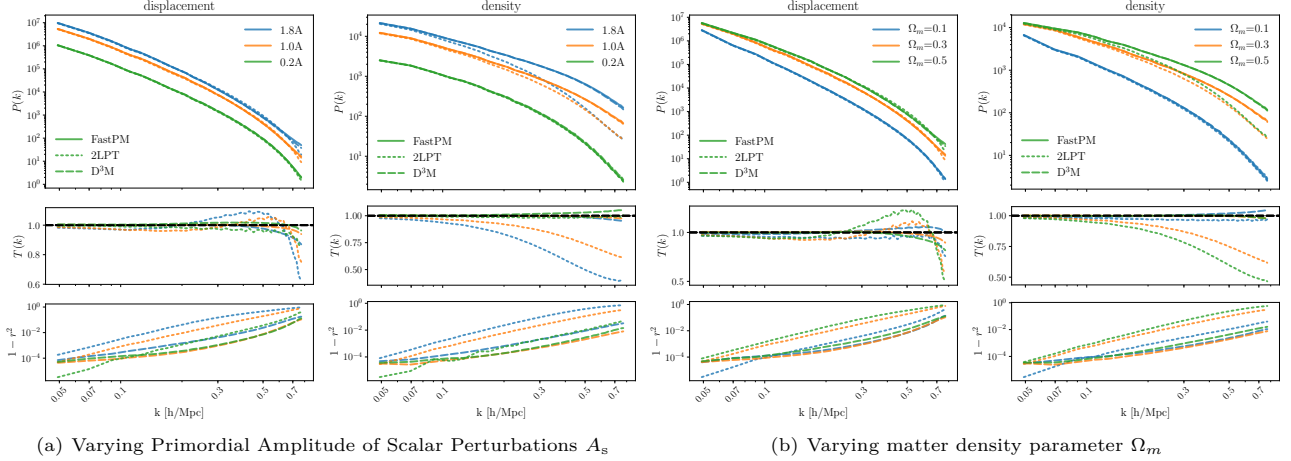


Fig. 5. Similar plots as in Figure 3(a). From top to bottom: the average power spectrum, transfer function and correlation coefficient for D³M and 2LPT when testing on different (a) A_s and, (b) Ω_m . D³M prediction outperforms 2LPT prediction at all scales except for the largest scales.

results confirm our expectation that increasing A_s increases the non-linearity of the structure formation process. While 2LPT can predict fairly well in linear regimes, its performance deteriorates as compared to D³M with increased non-linearity. It is interesting to note that D³M prediction maintains its advantage despite being trained on data from more linear regimes.

Varying matter density parameter Ω_m . We repeat the same experiments, this time changing Ω_m to 0.5 and 0.1, where the model is trained on $\Omega_m = 0.3089$, which is quite far from both of the test sets. The relative residual displacement error of the D³M (2LPT) averaged over 1000 simulations is 3.8% (15.2%) and 2.5% (4.3%) respectively. Figures 5(c)(d) show the two-point statistics for different values of Ω_m . For $\Omega_m = 0.5$, the results show that the D³M outperforms 2LPT at all scales, while for smaller $\Omega_m = 0.1$, D³M outperforms 2LPT on smaller scales ($k > 0.1$ h/Mpc). As for the 3PCF of different values of Ω_m , the mean relative 3PCF residual of deep learning model (2LPT) for $\Omega_m = 0.5$ and $\Omega_m = 0.1$ are 1.7% (7.6%) and 1.2% (1.7%) respectively. The D³M prediction performs better at $\Omega_m = 0.5$ than $\Omega_m = 0.1$. This is also because the universe is much more non-linear at $\Omega_m = 0.5$ than $\Omega_m = 0.1$. There is much more non-linearity to learn that are not modeled with 2LPT.

Conclusions

D³M can predict accurately the large-scale structure of Universe represented by our input simulations (FastPM) at all scales as seen in Table 1. Furthermore, D³M also performs better than our benchmark model (2LPT) at most scales, in terms of point-wise comparison, 2- and 3-point correlations. Finally, to our surprise, our model also generalizes well to test simulations with cosmological parameters (A_s and Ω_m) different from the training set (Table 1).

This indicates the deep learning model has the potential for deployment for producing a broader range of simulations beyond the parameter space covered by the training data. All results demonstrate that the D³M successfully learns the nonlinear mapping from first order perturbation theory to

		$T(k)$	$r(k)$	$T(k)$	$r(k)$	
	point-wise	$k = 0.11 \text{ h/Mpc}$	$k = 0.11 \text{ h/Mpc}$	$k = 0.51 \text{ h/Mpc}$	$k = 0.51 \text{ h/Mpc}$	3PCF
test phase						
2 LPT Density	N/A	0.96	1.00	0.73	0.94	0.0782
D ³ M Density	N/A	1.00	1.00	0.99	1.00	0.0079
2 LPT Displacement	0.093	0.96	1.00	1.04	0.89	N/A
D ³ M Displacement	0.028	1.00	1.00	0.99	1.00	N/A
$A_s = 1.8A_0$						
2LPT Density	N/A	0.93	1.00	0.49	0.78	0.243
D ³ M Density	N/A	1.00	1.00	0.98	1.00	0.039
2LPT Displacement	0.155	0.97	1.00	1.07	0.73	N/A
D ³ M Displacement	0.039	1.00	1.00	0.97	0.99	N/A
$A_s = 0.2A_0$						
2LPT Density	N/A	0.99	1.00	0.98	0.99	0.024
D ³ M Density	N/A	1.00	1.00	1.03	1.00	0.022
2LPT Displacement	0.063	0.99	1.00	0.95	0.98	N/A
D ³ M Displacement	0.036	1.00	1.00	1.01	1.00	N/A
$\Omega_m = 0.5$						
2LPT Density	N/A	0.94	1.00	0.58	0.87	0.076
D ³ M Density	N/A	1.00	1.00	1.00	1.00	0.017
2LPT Displacement	0.152	0.97	1.00	1.10	0.80	N/A
D ³ M Displacement	0.038	1.00	1.00	0.98	0.99	N/A
$\Omega_m = 0.1$						
2LPT Density	N/A	0.97	1.00	0.96	0.99	0.017
D ³ M Density	N/A	0.99	1.00	1.04	1.02	0.012
2LPT Displacement	0.043	0.97	1.00	0.97	0.98	N/A
D ³ M Displacement	0.025	0.99	1.00	1.02	1.00	N/A

Table 1. A summary of our analysis using different approximate N-body methods, fields and error measures.

FastPM simulation beyond what higher order perturbation theories can achieve.

We have no reason to believe that replacing FastPM with exact N-body simulations will deteriorate the performance of our method. Moreover, since the complexity of D³M is linear in the number of voxels, we expect to be able to further improve our encouraging results when moving to higher resolutions.

Laws of physics often respects large symmetry groups, which lead to nearly unique sets of equations (65). Similarly, after factoring out equivalence, one would expect that few distinct ML models will describe a physical law at the data level. We look forward to developing further in these directions towards interpretability of our deep models.

Materials and Methods

Dataset. The full simulation data consists of 10,000 ZA-FastPM simulation boxes as input-output pairs, with an effective volume of 20 (Gpc/h)^3 ($190 \times 10^9 \text{ ly}^3$), comparable to the volume of a large spectroscopic sky survey like DESI or EUCLID. We split the full simulation data set into 80%, 10%

and 10% for training, validation and test, respectively. We also generated 1000 simulations for 2LPT for each set of tested cosmological parameters.

Model and Training. The D³M adopts the U-Net architecture (51) with 15 convolution-deconvolution layers and approximately 8.4×10^6 trainable parameters. Our D³M generalizes the standard U-Net architecture to work with three-dimensional data.

Padding and Periodic Boundary. It is common to use constant or reflective padding in deep models for image processing. However, these approaches are not suitable for our setting. The physical model we are learning is constructed on a spatial volume with a periodic boundary condition. This is sometimes also referred to a torus geometry, where the boundaries of the simulation box are topologically connected – that is $x_{i+L} = x_i$ where i is the index of the spatial location, and L is the periodicity (size of box). Constant or reflective padding strategies break the connection between the physically nearby points separated across the box, which not only loses information but also introduces noise during the convolution, further aggravated with increased number of layers.

We find that the periodic padding strategy significantly improves the performance and expedites the convergence of our model, comparing to the same network using a constant padding strategy. This is not surprising, as one expects it is easier to train a model that can explain the data than to train a model that does not.

Loss Function and Training. We train the D³M to minimize the mean square error on particle displacements

$$\mathcal{L} = \frac{1}{N} \sum_i (\hat{\Psi}_i - \Psi_{t,i})^2, \quad [6]$$

where i labels the particles and the N is the total number of particles. This loss function is proportional to the integrated squared error, that in the Fourier space can be rewritten using the Parseval's theorem as

$$\int (\hat{\Psi} - \Psi_t)^2 d^3q = \int |\hat{\Psi} - \Psi_t|^2 d^3k = \int d^3k \left(|\Psi_t|^2 (1-T)^2 + 2|\hat{\Psi}||\Psi_t|(1-r) \right) \quad [7]$$

where \mathbf{q} is the Lagrangian space position, and \mathbf{k} is its corresponding wavevector. T is the transfer function defined in Eq. 2, and r is the correlation coefficient defined in Eq. 3. They characterize the similarity between the predicted and the true fields, in amplitude and phase respectively. Eq. 7 shows that our simple loss function jointly captures both of these measures; as T and r approach 1, the loss function approaches 0.

In the training phase, we employ the Adam Optimizer (66) with a learning rate of 0.0001, and first and second moment exponential decay rate of 0.9 and 0.999, respectively. We use the L2 regularization with regularization coefficient 0.0001.

Details of the D³M Architecture. The contracting path follows the typical architecture of a convolution network. It consists of two blocks, each of which consists of two successive convolutions of stride 1 and a down-sampling convolution with stride 2. The

convolution layers use $3 \times 3 \times 3$ filters with a periodic padding of size 1 (see Padding and Periodic Boundary) on both sides of each dimension. The padding ensures that the first two layers keep the shape of each channel. The following down-sampling layer reduces the shape of the layer by half on each spatial dimension. Notice that at each of the two down-sampling steps, we double the number of feature channels. At the bottom of the D³M, another two successive convolutions with stride 1 and the same periodic padding as above are applied. The expansive path of our D³M is an inverted version of the contracting path of the network. (It includes two repeated applications of the expansion block, each of which consists of one up-sampling transposed convolution with stride 1/2 and two successive convolution of stride 1. The transposed convolution and the convolution are constructed with $3 \times 3 \times 3$ filters.)

We take special care in the padding and cropping procedure to preserve the shifting and rotation symmetry in the up-sampling layer in expansive path. We apply before the transposed convolution a periodic padding of length 1 on the right, down and back sides of the box (`padding=(0,1,0,1,0,1)` in pytorch), and after the transposed convolution, we discard one column on the left, up and front sides of the box and two columns on the right, down and back sides (`crop=(1,2,1,2,1,2)`).

A special feature of the D³M is the concatenation procedure, where the up-sampling layer halves the feature channels and then concatenates them with the corresponding feature channels on the contracting path, doubling the number of feature channels.

The expansive building block then follows a $1 \times 1 \times 1$ convolution without padding, which converts the 64 features to the final 3-D displacement field. All convolutions in the network except the last one are followed by a rectified linear unit (ReLU) activation and batch normalization (BN).

ACKNOWLEDGMENTS. We thank Angus Beane, Peter Braam, Gabriella Contardo, David Hogg, Laurence Levasseur, Pascal Riposte and David Spergel for useful suggestions and comments, Angus Beane for comments on the paper, Nick Carriero for help on CCA computing clusters. The FastPM simulations are generated on the computer cluster Edison at the National Energy Research Scientific Computing Center (NERSC), a U.S. Department of Energy Office of Science User Facility operated under Contract No. DE-AC02-05CH11231. The training of neural network model is performed on the CCA computing facility and CMU AutonLab computing facility. The open source software toolkit `nbodykit` (67) is employed for the clustering analysis. YL acknowledges support from the Berkeley Center for Cosmological Physics and the Kavli IPMU established by World Premier International Research Center Initiative (WPI) of the MEXT, Japan. S.Ho thanks NASA for their support in grant number: NASA grant 15-WFIRST15-0008 and NASA ROSES grant 12-EUCLID12-0004.

References

1. Bond JR, Kofman L, Pogosyan D (1996) How filaments of galaxies are woven into the cosmic web. *Nature* 380:603–606.
2. Colless, M., et al. (2001) The 2dF Galaxy Redshift Survey: Spectra and redshifts. *Mon. Not. Roy. Astron. Soc.* 328:1039.
3. Eisenstein, D.J., et al. (2011) SDSS-III: Massive Spectroscopic Surveys of the Distant Universe, the Milky Way Galaxy, and Extra-Solar Planetary Systems. *Astron. J.* 142:72.
4. Jones, H.D., et al. (2009) The 6dF Galaxy Survey: Final Redshift Release (DR3) and Southern Large-Scale Structures. *Mon. Not. Roy. Astron. Soc.* 399:683.
5. Liske, J., et al. (2015) Galaxy and mass assembly (gama): end of survey report and data release 2. *Monthly Notices of the Royal Astronomical Society* 452(2):2087.
6. Scodeggio, M., et al. (2016) The VIMOS Public Extragalactic Redshift Survey (VIPERS). Full spectroscopic data and auxiliary information release (PDR-2). *ArXiv e-prints*.

7. Ivezić Ž, et al. (2008) LSST: from Science Drivers to Reference Design and Anticipated Data Products. *ArXiv e-prints*.
8. Amendola L, et al. (2018) Cosmology and fundamental physics with the Euclid satellite. *Living Reviews in Relativity* 21:2.
9. Green J, et al. (2012) Wide-Field InfraRed Survey Telescope (WFIRST) Final Report. *ArXiv e-prints*.
10. Davis M, Efstathiou G, Frenk CS, White SDM (1985) The evolution of large-scale structure in a universe dominated by cold dark matter.
11. LeCun Y, Bengio Y, Hinton G (2015) Deep learning. *nature* 521(7553):436.
12. Huang G, Liu Z, Van Der Maaten L, Weinberger KQ (2017) Densely connected convolutional networks. in *CVPR*. Vol. 1, p. 3.
13. Karras T, Aila T, Laine S, Lehtinen J (2017) Progressive growing of gans for improved quality, stability, and variation. *arXiv preprint arXiv:1710.10196*.
14. Gulrajani I, Ahmed F, Arjovsky M, Dumoulin V, Courville AC (2017) Improved training of wasserstein gans in *Advances in Neural Information Processing Systems*. pp. 5767–5777.
15. Van Den Oord A, et al. (2016) Wavenet: A generative model for raw audio. *CoRR abs/1609.03499*.
16. Amodei D, et al. (2016) Deep speech 2: End-to-end speech recognition in english and mandarin in *International Conference on Machine Learning*. pp. 173–182.
17. Hu Z, Yang Z, Liang X, Salakhutdinov R, Xing EP (2017) Toward controlled generation of text. *arXiv preprint arXiv:1703.00955*.
18. Vaswani A, et al. (2017) Attention is all you need in *Advances in Neural Information Processing Systems*. pp. 5998–6008.
19. Denton E, Fergus R (2018) Stochastic video generation with a learned prior. *arXiv preprint arXiv:1802.07687*.
20. Donahue J, et al. (2015) Long-term recurrent convolutional networks for visual recognition and description in *Proceedings of the IEEE conference on computer vision and pattern recognition*. pp. 2625–2634.
21. Silver D, et al. (2016) Mastering the game of go with deep neural networks and tree search. *nature* 529(7587):484.
22. Mnih V, et al. (2015) Human-level control through deep reinforcement learning. *Nature* 518(7540):529.
23. Levine S, Finn C, Darrell T, Abbeel P (2016) End-to-end training of deep visuomotor policies. *The Journal of Machine Learning Research* 17(1):1334–1373.
24. Ching T, et al. (2018) Opportunities and obstacles for deep learning in biology and medicine. *Journal of The Royal Society Interface* 15(141):20170387.
25. Alipanahi B, Delong A, Weirauch MT, Frey BJ (2015) Predicting the sequence specificities of dna- and rna-binding proteins by deep learning. *Nature biotechnology* 33(8):831.
26. Segler MH, Preuss M, Waller MP (2018) Planning chemical syntheses with deep neural networks and symbolic ai. *Nature* 555(7698):604.
27. Gilmer J, Schoenholz SS, Riley PF, Vinyals O, Dahl GE (2017) Neural message passing for quantum chemistry. *arXiv preprint arXiv:1704.01212*.
28. Carleo G, Troyer M (2017) Solving the quantum many-body problem with artificial neural networks. *Science* 355(6325):602–606.
29. Adam-Bourdarios C, et al. (2015) The higgs boson machine learning challenge in *NIPS 2014 Workshop on High-energy Physics and Machine Learning*. pp. 19–55.
30. He S, Ravanbakhsh S, Ho S (2018) Analysis of cosmic microwave background with deep learning.
31. Perraudin N, Defferrard M, Kacprzak T, Sgier R (2018) Deepsphere: Efficient spherical convolutional neural network with healpix sampling for cosmological applications. *arXiv preprint arXiv:1810.12186*.
32. Caldeira J, et al. (2018) Deepcmb: Lensing reconstruction of the cosmic microwave background with deep neural networks. *arXiv preprint arXiv:1810.01483*.
33. Ravanbakhsh S, et al. (2017) Estimating cosmological parameters from the dark matter distribution. *ArXiv e-prints*.
34. Mathuriya A, et al. (2018) Cosmoflow: using deep learning to learn the universe at scale. *arXiv preprint arXiv:1808.04728*.
35. Hezaveh, Y. D., Levasseur, L. P., Marshall, P. J. (2017) Fast automated analysis of strong gravitational lenses with convolutional neural networks. *Nature* 548:555–557.
36. Lanusse, F., et al. (2018) Cmu deeplens: deep learning for automatic image-based galaxy-galaxy strong lens finding. *MNRAS* pp. 3895–3906.
37. Kennerman N, Kirkby D, Ihler A, Sanchez-Lopez FJ (2018) ContextNet: Deep learning for star galaxy classification in *Proceedings of the 35th International Conference on Machine Learning*, Proceedings of Machine Learning Research, eds. Dy J, Krause A. (PMLR, Stockholm, Stockholm Sweden), Vol. 80, pp. 2582–2590.
38. Kim EJ, Brunner RJ (2016) Star-galaxy classification using deep convolutional neural networks. *Monthly Notices of the Royal Astronomical Society* p. stw2672.
39. Lochner M, McEwen JD, Peiris HV, Lahav O, Winter MK (2016) Photometric supernova classification with machine learning. *The Astrophysical Journal Supplement Series* 225(2):31.
40. Battaglia PW, Hamrick JB, Tenenbaum JB (2013) Simulation as an engine of physical scene understanding. *Proceedings of the National Academy of Sciences* p. 201306572.
41. Battaglia P, Pascanu R, Lai M, Rezende DJ, et al. (2016) Interaction networks for learning about objects, relations and physics in *Advances in neural information processing systems*. pp. 4502–4510.
42. Mottaghi R, Bagherinezhad H, Rastegari M, Farhadi A (2016) Newtonian scene understanding: Unfolding the dynamics of objects in static images in *Proceedings of the IEEE Conference on Computer Vision and Pattern Recognition*. pp. 3521–3529.
43. Chang MB, Ullman T, Torralba A, Tenenbaum JB (2016) A compositional object-based approach to learning physical dynamics. *arXiv preprint arXiv:1612.00341*.
44. Wu J, Yildirim I, Lim JJ, Freeman B, Tenenbaum J (2015) Galileo: Perceiving physical object properties by integrating a physics engine with deep learning in *Advances in neural information processing systems*. pp. 127–135.
45. Wu J, Lim JJ, Zhang H, Tenenbaum JB, Freeman WT (2016) Physics 101: Learning physical object properties from unlabeled videos. in *BMVC*. Vol. 2, p. 7.
46. Watters N, et al. (2017) Visual interaction networks: Learning a physics simulator from video in *Advances in Neural Information Processing Systems*. pp. 4539–4547.
47. Lerer A, Gross S, Fergus R (2016) Learning physical intuition of block towers by example. *arXiv preprint arXiv:1603.01312*.
48. Agrawal P, Nair AV, Abbeel P, Malik J, Levine S (2016) Learning to poke by poking: Experiential learning of intuitive physics in *Advances in Neural Information Processing Systems*. pp. 5074–5082.
49. Fragkiadaki K, Agrawal P, Levine S, Malik J (2015) Learning visual predictive models of physics for playing billiards. *arXiv preprint arXiv:1511.07404*.
50. Tompson J, Schlachter K, Sprechmann P, Perlin K (2016) Accelerating eulerian fluid simulation with convolutional networks. *arXiv preprint arXiv:1607.03597*.
51. Ronneberger, O.; Fischer P, Brox T (2015) U-Net: Convolutional Networks for Biomedical Image Segmentation.
52. Zel'dovich YB (1970) Gravitational instability: An approximate theory for large density perturbations.
53. White M (2014) The Zel'dovich approximation. *MNRAS* 439:3630–3640.
54. Feng Y, Chu MY, Seljak U, McDonald P (2016) FASTPM: a new scheme for fast simulations of dark matter and haloes.
55. Buchert T (1994) Lagrangian Theory of Gravitational Instability of Friedman-Lemaître Cosmologies - a Generic Third-Order Model for Nonlinear Clustering.
56. Jasche J, Wandelt BD (2013) Bayesian physical reconstruction of initial conditions from large-scale structure surveys. *MNRAS* 432:894–913.
57. Kitaura FS (2013) The initial conditions of the Universe from constrained simulations. *MNRAS* 429:L84–L88.
58. Dawson KS, et al. (2013) The Baryon Oscillation Spectroscopic Survey of SDSS-III. *AJ* 145:10.
59. Dawson KS, et al. (2016) The SDSS-IV Extended Baryon Oscillation Spectroscopic Survey: Overview and Early Data. *AJ* 151:44.
60. DESI Collaboration, et al. (2016) The DESI Experiment Part I: Science, Targeting, and Survey Design. *ArXiv e-prints*.
61. Feng Y, Seljak U, Zaldarriaga M (2018) Exploring the posterior surface of the large scale structure reconstruction. *J. Cosmology Astropart. Phys.* 7:043.
62. Chan KC (2014) Helmholtz decomposition of the Lagrangian displacement.
63. Slepian Z, Eisenstein DJ (2015) Computing the three-point correlation function of galaxies in $\mathcal{O}(N^2)$ time.
64. Planck Collaboration, et al. (2016) Planck 2015 results. XIII. Cosmological parameters.
65. Mallat S (2016) Understanding deep convolutional networks. *Philosophical Transactions of the Royal Society A: Mathematical, Physical and Engineering Sciences* 374:20150203.
66. Kingma D, Ba J (2014) Adam: A method for stochastic optimization.
67. Hand N, et al. (2018) nbodykit: an open-source, massively parallel toolkit for large-scale structure. *The Astronomical Journal* 156(4):160.